TRENDS IN SCIENCES 2026; 23(1): 11067
https://doi.org/10.48048/tis.2026.11067 RESEARCH ARTICLE

Valorization of Moringa Oleifera Stem into Activated Carbon for Dye Removal: Coupled Effects of Lignocellulosic Composition and Pyrolysis Temperature

Widi Astuti[1,*], Irene Nindita Pradnya[1], Triastuti Sulistyaningsih[2], Luluk Arvi Cahyaning Suwandi[1], Afifah Sagita Fitria Wati[1], Erwan Adi Saputro[3] and Zulfa Ajrina Fitri[4]

[1]Departement of Chemical Engineering, Universitas Negeri Semarang, Semarang, Indonesia
[2]Department of Chemistry, Universitas Negeri Semarang, Semarang, Indonesia
[3]Department of Chemical Engineering, Universitas Pembangunan Nasional "Veteran" Jawa Timur, Surabaya, Indonesia
[4]School of Agriculture, Food, and Ecosystem Sciences, Faculty of Science, The University of Melbourne, Victoria, Australia

([*]Corresponding author's e-mail: widi_astuti@mail.unnes.ac.id)

Received: 25 July 2025, Revised: 31 July 2025, Accepted: 7 August 2025, Published: 25 October 2025

Abstract

Moringa oleifera stem (MOS) waste contains 30.61% cellulose, 27.37% hemicellulose, and 20.78% lignin, making it a promising precursor for biochar and activated carbon (AC) production. However, the high lignin and cellulose contents may contribute to significant tar formation during pyrolysis, resulting in pore blockage and reduced carbon material quality. This study investigates the coupled effects of lignocellulosic composition (i.e., cellulose, hemicellulose, and lignin) and pyrolysis temperature on the surface chemistry, microstructural characteristics, and adsorption performance of the resulting AC. Pyrolysis of MOS powder was carried out in a muffle furnace under limited air conditions at 2 target temperatures: 500 °C (denoted as MOSbc-500) and 600 °C (denoted as MOSbc-600). Chemical activation was subsequently performed using potassium hydroxide (KOH) at a mass ratio of 3:1 (KOH:biochar) in a muffle furnace under limited air conditions at 800 °C. Surface morphology was examined using SEM equipped with EDX, while the surface functional groups were characterized via FTIR spectroscopy. The pore structure was analyzed through N_2 adsorption-desorption measurements. The results indicate that the surface of MOSbc-600 appears cleaner than that of MOSbc-500, suggesting reduced tar deposition at the higher pyrolysis temperature. The AC derived from MOSbc-600 (denoted as MOSac-600) exhibited higher oxygen-containing functional groups compared to that derived from MOSbc-500 (denoted as MOSac-500). Moreover, MOSac-600 demonstrated a higher BET surface area (1221.56 m^2/g) and an average mesopore diameter of 3.42 nm, contributing to a high methyl violet (MV) adsorption capacity of 29.94 mg/g at pH 11. Equilibrium adsorption data were best described by the Langmuir isotherm model. These findings suggest that MOS-derived AC is a low cost, high removal efficiency, and environmentally sustainable adsorbent with significant potential for wastewater treatment applications.

Keywords: Adsorbent, Biochar, Langmuir isotherm, Lignocellulose, Methyl violet, Tar, Wastewater treatment

Introduction

Rapid industrialization has led to a significant increase in water pollution, posing serious threats to both human health and ecological systems. Wastewater generated by industries such as textiles, ink, leather, paper, and paint contains a wide range of synthetic dyes. These dyes are often resistant to biodegradation due to their complex chemical structures, which frequently include substituted chromophore groups such as azo,

triarylmethane, and anthraquinone [1]. Synthetic dyes are generally classified into 3 categories: Cationic, anionic, and non-ionic, with cationic dyes typically regarded as the most hazardous. Methyl violet (MV), a highly toxic cationic dye, is commonly detected in industrial effluents owing to its widespread use in the paint and textile industries. Due to its high toxicity and environmental persistence, the presence of MV in aquatic ecosystems poses significant ecological and public health risks, underscoring the need for its efficient removal from wastewater [1]. Various treatment technologies have been developed to eliminate hazardous dyes from wastewater, including coagulation and precipitation [2], photocatalytic degradation [3], electrochemical oxidation [4], ozonation [5], micellar enhanced ultrafiltration [6], membrane separation process [7], and adsorption [8,9]. Among these, adsorption is particularly advantageous due to its operational simplicity, cost-effectiveness, high removal efficiency [10], effectiveness at low contaminant concentrations, rapid adsorption kinetics, and environmental sustainability [11].

Several low-cost adsorbents have been extensively investigated, including clay [5,6], chitosan [7], lignocellulosic waste [12], bentonite [13], and various types of activated carbon (AC) [14]. Among these, AC is widely regarded as a promising adsorbent for dye removal from wastewater [8], primarily due to its large surface area, high porosity, high adsorption capacity, and the presence of diverse surface functional groups, which can be chemically modified to enhance adsorption performance [11]. However, the relatively high production cost of AC has limited its widespread application. To address this limitation, many agricultural wastes have been explored as alternative precursors for AC production, including cassava peel [8], pineapple leaf [9], and peanut shell [15]. The synthesis of the AC typically involves 2 main stages: pyrolysis and activation. During pyrolysis, lignocellulosic components, namely lignin, hemicellulose, and cellulose, undergo thermal decomposition at specific temperature ranges, producing biochar and volatile compounds [9]. The subsequent activation process, aimed at enhancing the surface area and porosity of the biochar, can be performed through either physical or chemical methods [8]. While physical activation is generally more cost-effective and environmentally friendly, chemical activation is often preferred due to its ability to open blocked pores, enlarge existing ones, and generate new pores. Additionally, chemical activation introduces surface functional groups that serve as active sites for chemisorption through electrostatic interactions or chemical bonding [9,15]. The precursor is mixed with activator such as KOH [8], H_3PO_4 [8,14], $ZnCl_2$ [9], K_2CO_3 [15], and NaOH [16]. Among these, KOH is particularly advantageous due to its effectiveness in developing micropores structures and introducing oxygen-containing functional groups on the surface [8]. Therefore, achieving the desired surface chemistry and porosity in AC requires optimized synthesis strategies that consider the precursor composition, pyrolysis conditions, and the activation method employed.

On the other hand, the exploration of plant biodiversity that demonstrates both resilience to extreme environmental conditions and alignment with the United Nations Sustainable Development Goals (SDGs) has become a key research priority. *Moringa oleifera*, a tropical plant native to India, is considered one of the most suitable candidates in this regard due to its remarkable adaptability; it thrives in both humid tropical climates and arid, nutrient-deficient soils [17]. Various parts of the plant, including leaves, stem, and seeds, are rich in antioxidants such as flavonoids, polyphenols, niazirins, and isothiocyanates [18], which contribute to its wide range of health-promoting properties. However, the extraction of these bioactive compounds generates solid residues that are often underutilized, such as moringa oleifera stem (MOS). Given that the agricultural and industrial sectors are among the largest global contributors to biowaste, the reduction and valorization of agro-industrial residues such as MOS are critical for advancing circular economy practices. The stem contains approximately 30.61% cellulose, 27.37% hemicellulose, and 20.78% lignin, making it a promising precursor to produce AC. During biomass pyrolysis, cellulose, hemicellulose, and lignin decompose at different rates and over distinct temperature ranges. Consequently, the yield and characteristics of the resulting AC are influenced not only by the intrinsic properties and composition of the precursor material but also by the specific pyrolysis conditions and activation methods employed. Despite its potential, the combined effects of lignocellulosic composition and pyrolysis

temperature on the surface chemistry, microstructure, and adsorption performance of AC derived from MOS remain underexplored. This gap highlights the need for systematic studies aimed at optimizing both AC yield and quality. Such investigations are essential for fine-tuning pyrolysis parameters to achieve the desired physicochemical characteristics of the final product. In this context, MOS was selected as a precursor primarily due to its high content of 3 major biopolymers (e.g., lignin, cellulose, and hemicellulose) enabling the observation of significant changes in physicochemical properties under varying pyrolysis conditions. Additionally, the potential of MOS-derived AC for MV adsorption was also evaluated. Key operational parameters, including pH, contact time, and initial dye concentration, were investigated. Furthermore, equilibrium studies were also conducted to determine essential parameters for adsorption process design [8,9].

Materials and methods

Materials and reagents

MOS waste was collected from a local market in Gunungpati, Semarang, Indonesia. All other chemicals used in this study, including methyl violet 2B ($C_{24}H_{28}N_3Cl$), potassium hydroxide (KOH), natrium hydroxide (NaOH), and hydrochloric acid (HCl) 37% were purchased from Sigma Aldrich (Germany).

Pretreatment of moringa oleifera stem

Prior to any treatment, the MOS was cut into small pieces and thoroughly washed with distilled water to remove impurities, followed by sun-drying. The dried material was then ground and sieved to obtain a uniform particle size of 60 mesh. The resulting MOS powder was further dried in an oven (UN55 Memmert, Germany) at 105 °C until a constant weight was achieved. The lignocellulosic composition of MOS, expressed on a dry weight basis, is presented in **Table 1**.

Table 1 Chemical composition of moringa oleifera stem and yields**.**

Samples	Chemical composition (%)			Biochar yield (%)		AC yield (%)	
	C [a]	HC [b]	L [c]	500 °C	600 °C	500 °C	600 °C
MOS	30.61	27.37	20.78	34.99	32.64	74.47	64.56

[a] C: Cellulose, [b] HC: Hemicellulose, [c] L: Lignin

Preparation of activated carbon

Pyrolysis of MOS powder was carried out in a ceramic muffle furnace (B-ONE BFNC-2-1200) under limited air conditions [9] at 2 target temperatures: 500 °C (denoted as MOSbc-500) and 600 °C (denoted as MOSbc-600). A temperature of 500 °C was achieved within 43 min and 600 °C within 51 min, both corresponding to a heating rate of 0.2 °C/s. The samples were then held at their respective temperatures for 2 h to facilitate biochar formation. Chemical activation was subsequently performed using potassium hydroxide (KOH) at a mass ratio of 3:1 (KOH:Biochar). Specifically, 30 g of KOH was dissolved in 15 mL of distilled water and thoroughly mixed with 10 g of biochar. The mixture was stirred for 2 h and then dried in an electric oven (UN55, Memmert, Germany) at 105 °C until a constant weight was achieved. The dried impregnated biochar was then subjected to thermal activation in the same furnace (B-ONE BFNC-2-1200) under limited air at a target temperature of 800 °C. This temperature was attained within 65 min at a heating rate of 0.2 °C/s, and the samples were held at 800 °C for 1 h. Following activation, the resulting AC was washed with 0.1 M hydrochloric acid (HCl) and repeatedly rinsed with distilled water until a neutral pH was achieved. The final product was then dried again at 105 °C until a constant weight was obtained. The AC derived from MOSbc-500 and MOSbc-600 were denoted as MOSac-500 and MOSac-600, respectively. Biochar yield was calculated as the ratio of the mass of biochar obtained after pyrolysis to the mass of the dried raw biomass, as expressed in Eq. (1). Similarly, the AC yield was determined as the ratio of the mass of AC obtained after KOH activation to the mass of biochar prior to activation, as expressed in Eq. (2) [8,9]. The results are summarized in **Table 1**.

$$Y_{bc} = \frac{M_{bc}}{M_{db}} \times 100\% \quad (1)$$

$$Y_{ac} = \frac{M_{ac}}{M_{bc}} \times 100\% \quad (2)$$

where Y_{bc} (%) represents the biochar yield, Y_{ac} (%) the AC yields, M_{bc} (g) the mass of biochar, M_{db} (g) the mass of dried biomass, and M_{ac} (g) the mass of AC.

Characterization of materials

The pore structure of the AC was analyzed using a QuantaChrome Nova 1200 analyzer through nitrogen (N_2) adsorption-desorption measurements at 77 K. The surface area was determined using the Brunauer-Emmett-Teller (BET) method within a relative pressure range of 0.001 - 0.300 kg/cm^2. Pore size distribution (PSD) was evaluated using the Barret Joiner Halenda (BJH) methods. Thermal stability was assessed via thermogravimetric analysis (TGA) using a Linseis STA PT 1600 analyzer (Germany) under a nitrogen atmosphere at a flow rate of 100 mL/min. The samples were heated from ambient temperature to 600 °C at a rate of 10 °C/min. The surface morphology of the biochar and AC samples was characterized using a scanning electron microscope (SEM) equipped with energy-dispersive X-ray (EDX) spectroscopy (Phenom ProX Desktop, UK). Functional groups were identified using Fourier Transform Infrared (FTIR) spectroscopy (Perkin Elmer, USA) over a wavenumber range of 4,000 to 400 cm^{-1}. Samples were prepared as potassium bromide (KBr) pellets, and functional groups were identified based on their characteristic absorption bands.

Adsorption studies

Adsorption experiments were conducted to evaluate the effects of solution pH, contact time, and initial MV concentration. The effect of pH was investigated over a range of 1 to 11 using a 100 mg/L MV solution. pH adjustments were made using 0.1 M HCl and 0.1 M NaOH solutions. The influence of contact time was assessed over a period of 0 to 180 min at pH 11, also using a 100 mg/L MV solution. For isotherm studies, the initial MV concentration was varied from 5 to 500 mg/L, with all experiments conducted at pH 11 and a contact time of 180 min. In each experiment, 0.5 g of AC was added to 50 mL of MV solution. The mixtures were agitated at 200 rpm using an Innova 2,100 shaker under ambient conditions to ensure effective adsorption. Following the adsorption process, suspended solids were separated by filtration, and the filtrates were analyzed for residual MV concentration using a UV-Visible spectrophotometer (Genesys 10 UV, Thermo Scientific, USA) at a maximum wavelength (λ_{max}) of 590 nm. The amount of MV adsorbed at equilibrium, q_e (mg/g), and at a given time, q_t (mg/g), was calculated using Eqs. (3) and (4), respectively [8,9]. The percentage of MV removal was determined using Eq. (5), as described in previous studies [8]:

$$q_e = \frac{(C_o - C_e)\,V}{m} \quad (3)$$

$$q_t = \frac{(C_o - C_t)\,V}{m} \quad (4)$$

$$\textit{methyl violet adsorbed (\%)} = \frac{(C_o - C_t)}{C_o} \times 100 \quad (5)$$

where C_o (mg/L) represents the initial concentration of the MV solution, C_e (mg/L) is the MV concentration in the liquid phase at equilibrium, m (g) denotes the adsorbent dose, V (L) is the volume of MV solution, and C_t (mg/L) is the concentration of MV in the liquid phase at a given time, t (min).

Results and discussion

Thermogravimetric analysis

During biomass pyrolysis, hemicellulose, cellulose, and lignin decompose over distinct temperature ranges due to differences in their chemical structures and thermal stabilities. Hemicellulose is an amorphous, branched heteropolymer primarily composed of pentoses (e.g., xylose, arabinose) and hexoses (e.g. mannose, glucose, galactose). It contains a relatively high proportion of oxygen-containing functional groups, particularly carboxylic (-COOH) and acetyl groups, which significantly influence its thermal decomposition behavior. Owing to its amorphous structure and lower degree of polymerization compared to cellulose, hemicellulose decomposes more rapidly and at lower temperatures, typically within the range of 200 - 315 °C. The thermal degradation of hemicellulose involves several key reactions, including dehydration, depolymerization, cleavage of acetyl groups (resulting in acetic acid release), decarboxylation (producing CO_2), and the formation of light oxygenated compounds

such as furfural, formic acid, methanol, acetol, and hydroxyacetaldehyde [19]. Compared to cellulose and lignin, hemicellulose produces a lower amount of char. In contrast, cellulose is a linear homopolymer composed of long chains of β-1,4-linked glucose units. During pyrolysis, cellulose undergoes depolymerization, with levoglucosan serving as the primary degradation product; dehydration reactions contribute to char and light oxygenated compounds formation; fragmentation and isomerization produce hydroxyacetaldehyde, acetol and formaldehyde; and cross-linking reactions leading to secondary char formation. The thermal degradation of cellulose generally occurs within the temperature range of 315 - 400 °C. Levoglucosan acts as a key intermediate and can further degrade into tar components rich in oxygenated compounds such as furfural, hydroxyacetaldehyde, formic acid, glycolaldehyde, and acetic acid [19]. At temperatures exceeding 400 °C, cellulose undergoes nearly complete decomposition, leaving minimal solid residue. Lignin, the most thermally stable component of lignocellulosic biomass, plays a crucial structural role in the plant cell wall. It is composed of a complex, 3-dimensional aromatic polymer formed from phenylpropane units linked through C-O-C and C-C bonds. Its relatively high carbon content (approximately 62%) compared to that of hemicellulose (44%), contributes to its greater char-forming potential [20]. Lignin degrades gradually degradation at temperature above 400 °C, producing non-condensable gases, biochar, and condensable tar compounds, such as phenol, guaiacol, and catechol [19]. The thermal degradation behavior of MOS was evaluated using TGA to determine the optimal pyrolysis temperature range for effective biochar production.

Figure 1(a) illustrates the thermogravimetric (TG) and derivative thermogravimetric (DTG) curves for MOS, showing the relationship between mass loss and the rate of mass change. The TG curve demonstrates a non-linear and progressive reduction in mass, occurring in 3 distinct stages. These stages correspond to the thermal degradation of the major biomass components: Hemicellulose, cellulose, and lignin, each exhibiting different thermal stabilities [20,21]. In the first stage, occurring below 220 °C, a mass loss of approximately 0.76% is observed, primarily attributed to the evaporation of moisture and low molecular weight volatile compounds. This initial loss indicates the presence of volatile components in the raw material that degrade under mild thermal conditions. The second stage, spanning 220 - 360 °C, is characterized by thermal decomposition of hemicellulose and cellulose, leading to the evolution of volatile compounds and non-condensable gases such as CO_2, CO, and H_2. This stage results in a significant mass loss of 54.3%. The third stage, occurring above 360 °C, involves the gradual, passive pyrolytic degradation of the remaining biomass, particularly lignin, resulting in a slower rate of mass loss as temperature increases. This stage is associated with biochar formation. Unlike the preceding stages, it does not exhibit a distinct degradation peak. Instead, the degradation rate progressively decreases and approaches an asymptote, indicating the slow and continuous breakdown of lignin. This stage contributes an additional mass loss of 32.8%. At the maximum experimental temperature of 600 °C, the total mass loss reached 87.9%, leaving a solid residue of 12.1%. This residual mass is lower than that observed at 500 °C, where 26.5% of the original mass remained. The residual fraction primarily consists of lignin-derived products, with minor contributions from the incomplete decomposition of hemicellulose and cellulose [19,22]. As cellulose is nearly completely pyrolyzed at temperatures above 400 °C, its contribution to the residual solid mass is minimal. Accordingly, higher lignin content correlates with increased char yield. For comparison, *Pithecellobium jiringa* peel, which contains a higher lignin content (42.47%) than MOS (20.78%), produced significantly higher solid residues 46.6% and 34.7% at pyrolysis temperatures of 500 and 600 °C, respectively (**Figure 1(b)**).

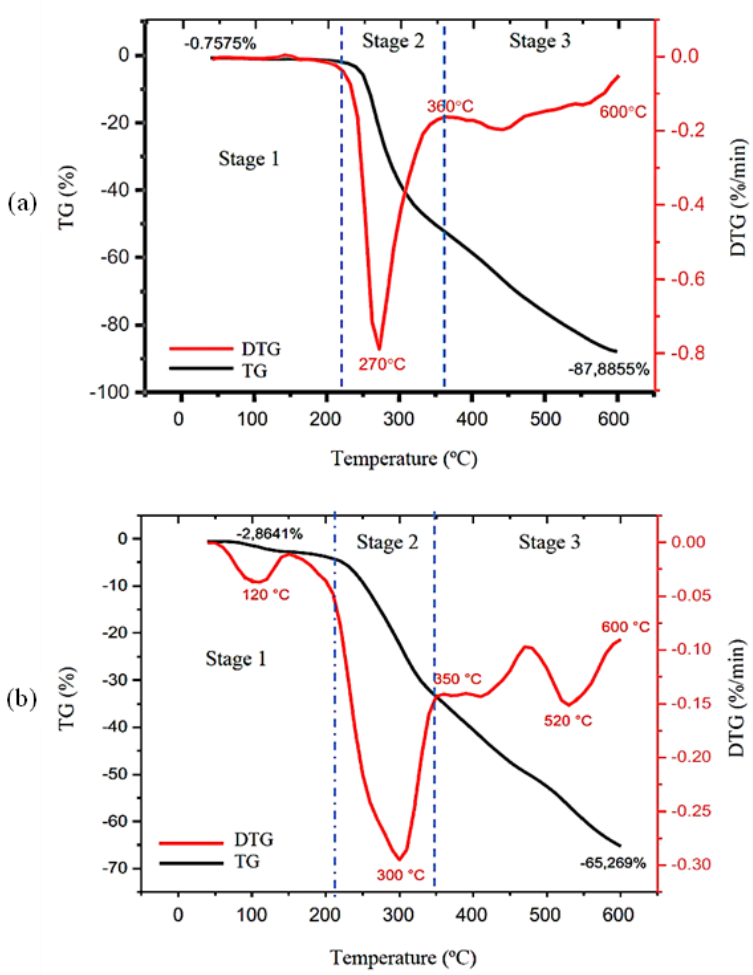

Figure 1 TG and DTG curve of (a) *Moringa oleifera* stem (MOS) and (b) *Pithecellobium jiringa* peel.

SEM-EDX analysis

Figure 2 presents SEM images of biochar and AC derived from MOS. The surface morphology of biochar (**Figures 2(a) - 2(d)**) exhibits a sheet-like structure with visible cracks and limited pore development. Although some pore frameworks are observable, they appear relatively shallow, likely due to the retention of volatile compounds and tar within carbon matrix. Tar is a complex mixture of condensable hydrocarbons, comprising single to 5 ring aromatic compounds, polycyclic aromatic hydrocarbons (PAHs), and various oxygen-containing hydrocarbons [19]. Based on their formation mechanisms and chemical composition, tars are generally classified into 3 categories: Primary, secondary, and tertiary tar. Primary tars, formed at pyrolysis temperatures ranging from 400 to 700 °C [19], primarily consist of oxygenated compounds derived from the thermal degradation of cellulose and lignin. Due to the high cellulose and lignin content in MOS (51.39%), significant tar deposition is observed on the surface of the biochar (**Figure 2(a)**). According to Xu *et al.* [22], tar formation peaks at approximately 500 °C. The primary reason for the higher tar yield at 500 °C compared to 400 °C is the intensified pyrolysis reactions at this temperature, which continuously generate tar. However, at temperature exceeding 500 °C, macromolecular organics within the tar undergo cracking reactions, such as demethylation, debranching, and decarboxylation. As a result, the surface of MOSbc-600 (**Figure 2(c)**) appears cleaner than that of MOSbc-500 (**Figure 2(a)**). This observation is supported by EDX analysis, which indicates a significantly lower abundance of oxygen (O) in MOSbc-600 (**Figure 3(c)**) compared to MOSbc-500 (**Figure 3(a)**). Additional evidence of tar accumulation on the surface of MOSbc-500 is provided by EDX data in **Figures 3(a) - 3(b)**. Notably, the higher oxygen content detected at point 1 (**Figure 3(a)**) relative to point 2 (**Figure 3(b)**) suggests the localized presence of oxygen-rich compounds on the surface of MOSbc-500. In addition to generating non-

condensable gases, some volatile compounds undergo secondary reactions with the biochar matrix, leading to the formation of secondary char and contributing to development of new pores or widening of existing ones. Consequently, the pore structure of MOSbc-600 is more developed, with several pores appearing more open and well-defined (**Figure 2(d)**).

This morphological enhancement is corroborated by BET surface area data **(Table 2)**, which indicate that both the BET surface area and porosity of MOSbc-600 are higher than those of MOSbc-500. The increase in porosity is accompanied by a slight reduction in yield, with MOSbc-600 exhibiting a lower biochar yield (32.64%) compared to MOSbc-500 (34.99%). Following the activation process (**Figures 2(e) - 2(h)**), the biochar surface displays increased roughness, fragmented sheet-like structures, more complex morphology, enhanced porosity, and a more irregular, folded appearance. A higher pyrolysis temperature (600 °C) results in a greater number and interconnectivity of pores, as shown in the SEM images (**Figures 2(g) - 2(h)**) and supported by data in **Table 2**. This enhancement in porosity at elevated temperature is also associated with a reduction in biochar yield, decreasing from 74.47% for MOSac-500 to 64.56% for MOSac-600, as presented in **Table 1**. These morphological transformations, particularly the increase in porosity and the development of complex, folded structures, are essential for increasing the number of accessible adsorption sites and facilitating intraparticle diffusion of adsorbate molecules, thereby enhancing adsorption efficiency and kinetics. During KOH activation process, thermal energy is absorbed by potassium (K) atoms impregnated within the biochar matrix, energizing them and facilitating their migration into internal structure of the carbon matrix [8]. This intercalation process facilitates the expansion and widening of existing pores. Upon continued heating, the intercalated K atoms are removed, resulting in the formation of a highly porous carbon structure. According to Astuti *et al.* [8], the development of porosity during KOH activation can be attributed to the reaction between carbon and KOH (C_f-KOH), as shown in Eqs. (6) - (14).

$$2\ KOH \rightarrow K_2O + H_2O \quad (6)$$

$$C_f + H_2O \rightarrow H_2 + CO \quad (7)$$

$$CO + H_2O \rightarrow H_2 + CO_2 \quad (8)$$

$$K_2O + C_f \rightarrow 2K + CO \quad (9)$$

$$K_2O + H_2 \rightarrow 2K + H_2O \quad (10)$$

$$K_2O + CO_2 \rightarrow K_2CO_3 \quad (11)$$

$$K_2CO_3 + 2\ C_f \rightarrow 2K + 3CO \quad (12)$$

$$K_2CO_3 \rightarrow K_2O + CO_2 \quad (13)$$

$$K_2O + 2\ C_f \rightarrow 2\ K + CO \quad (14)$$

Based on Eqs. (12) - (14), it can be concluded that K atoms are produced as a final product in the series of reactions that occur during the KOH activation process. Activation typically takes place at temperatures around 800 °C, while the boiling point of potassium is 759 °C [8]. Consequently, a significant portion of the potassium volatilizes during the subsequent heating phase following intercalation, escaping through the furnace ventilation and exhaust systems. This volatilization is supported by the low potassium content detected in the SEM-EDX analysis (**Figures 3(d)** and **3(e)**). Therefore, it can be inferred that the diffusion of potassium compounds into the internal structure of the biochar matrix contributes not only to the widening of existing pores, as previously described, but also to the formation of new pores through reactions between the carbon fraction (C_f) and potassium compounds.

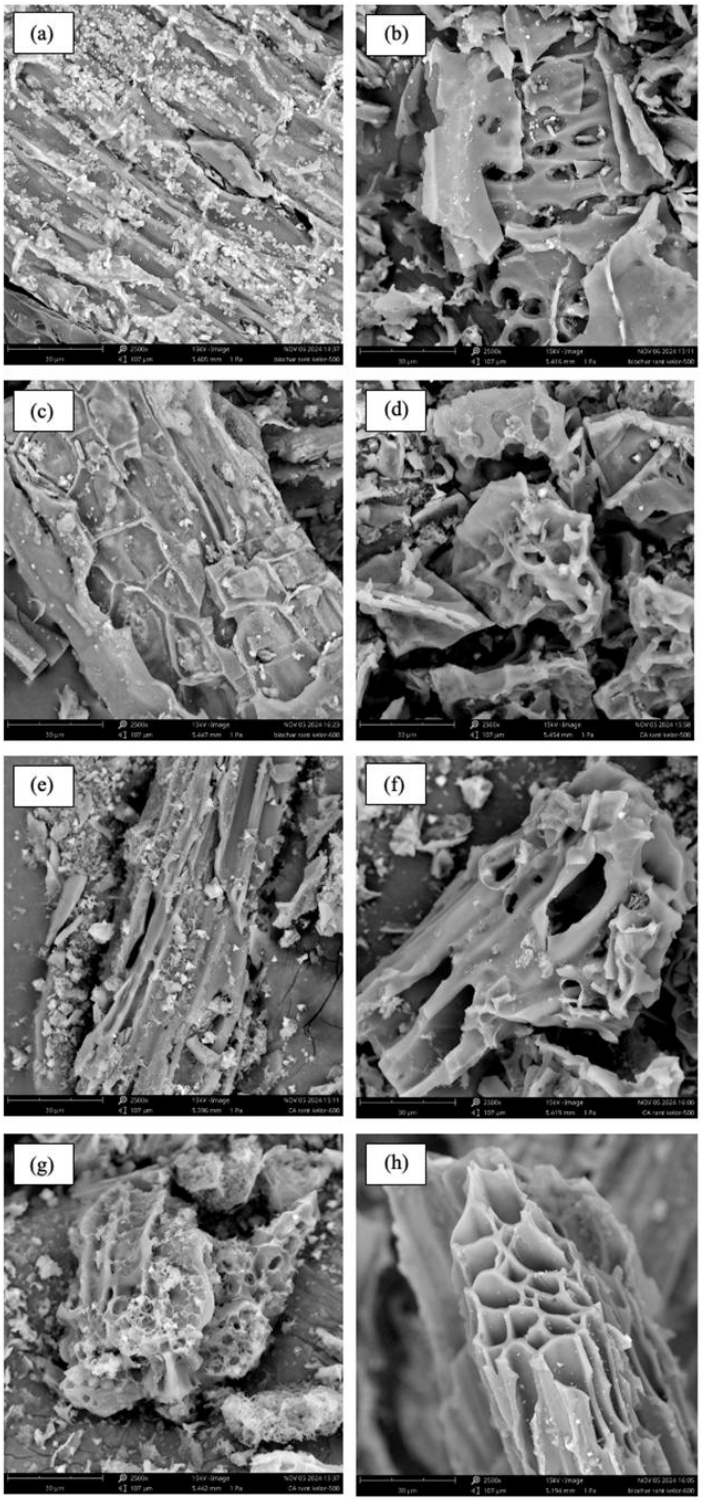

Figure 2 Scanning electron microscope (SEM) images of (a,b) MOSbc-500, (c) and (d) MOSbc-600, (e,f) MOSac-500, (g) and (h) MOSac-600.

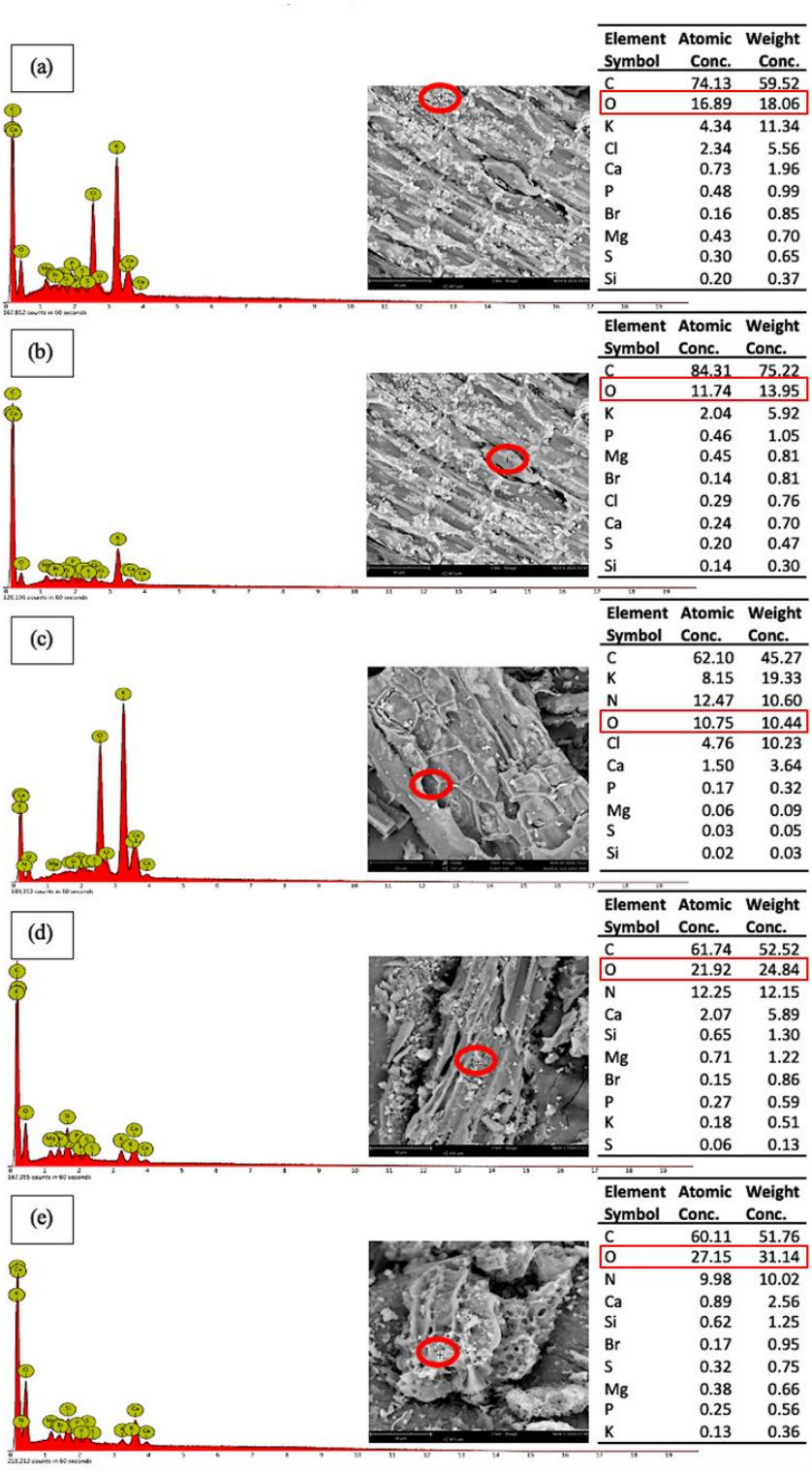

Figure 3 SEM-EDX images of (a,b) MOSbc-500, (c) MOSbc-600, (d) MOSac-500, and (e) MOSac-600.

Table 2 Surface physical characteristics of *Moringa oleifera* stem (MOS) char and activated carbon (AC).

Surface physical parameters	MOSbc-500	MOSbc-600	MOSac-500	MOSac-600
BET surface area (m^2/g)	11.75	53.91	800.53	1221.56
Micropore surface area (m^2/g)	7.090	30.90	646.72	967.05
Total pore volume (cm^3/g)	0.024	0.051	0.58	0.67

Surface physical parameters	MOSbc-500	MOSbc-600	MOSac-500	MOSac-600
Micropore volume (cm^3/g)	0.003	0.019	0.33	0.49
Micropore volume (%)	12.5	37.254	56.89	73.13
Pore radius (nm)	2.32	2.14	3.06	3.42

FTIR analysis

As previously discussed, the thermal decomposition of lignin and cellulose generates tar, an oxygenated compound capable of occluding the pores of pyrolytic biochar. In addition to being identified through SEM-EDX analysis, tar, typically composed of various oxygen-containing hydrocarbons and polycyclic aromatic hydrocarbons (PAHs), can also be detected via FTIR spectra [22]. The presence of oxygenated functional groups is indicated by characteristic absorption bands, including peaks around 3,630 cm^{-1}, corresponding to the O-H stretching vibration of free hydroxyl groups in phenolic and alcoholic compounds [23]; a peak near 3,445 cm^{-1}, attributed to the O-H stretching of hydrogen-bonded hydroxyl groups [23]; absorption in the 1,260 - 1,000 cm^{-1} region, associated with C-O or C-O-C symmetric stretching in esters, ethers, alcohols, and phenols [24]; and bands between 1,760 and 1,710 cm^{-1}, representing C=O stretching vibration. Meanwhile, the presence of PAHs is identified by absorption peaks near 1,600 cm^{-1}, corresponding to C=C stretching indicative of lignin and aromatic structures [24], and within the 870 - 750 cm^{-1} range, corresponding to aromatic C–H out-of-plane bending vibration [24]. Hemicellulose, which is primarily composed of pentoses and hexoses bearing oxygen-containing functional groups, particularly carboxyl groups (-COOH), can be identified by a broad absorption band around 3,300 cm^{-1}, corresponding to O-H stretching vibrations of the carboxylic groups, and by absorption in the range of 1,760 - 1,710 cm^{-1}, attributed to C=O stretching. As previously discussed, tar formation peaks at approximately 500 °C and declines at higher temperatures due to secondary reactions such as tar cracking. Simultaneously, carboxylic acid groups in hemicellulose undergo thermal decomposition, leading to the release of CO_2. The disappearance of O-H and C=O absorption bands in the FTIR spectra thus indicates the degradation and loss of carboxyl functionalities.

The surface chemical functional groups of biochar and AC samples in this study were characterized using FTIR spectroscopy, as shown in **Figure 4**. In **Figure 4(a)**, the FTIR spectrum of MOSbc-500 exhibits a broad absorption band in the range of 3,600 - 3,200 cm^{-1}, corresponding to O-H stretching vibrations of hydroxyl-containing functional groups such as phenols and alcohols. This band overlaps with another broad band centered around 3,300 cm^{-1}, typically attributed to the O-H stretching vibrations of carboxylic acid (-COOH) groups [23]. An absorption band near 1,700 cm^{-1} is indicative of C=O stretching vibrations, characteristic of carboxyl functionalities. The band observed in the 1,500 - 1,400 cm^{-1} region is associated with aromatic C=C stretching vibrations [24], suggesting the presence of lignin-derived aromatic ring structures. Additionally, the region between 1,300 and 900 cm^{-1} corresponds to C-O stretching vibrations from various overlapping surface functional groups, including ether groups (1,275 - 1,210 cm^{-1}), carboxylic groups (1,300 - 1,170 cm^{-1}), and phenolic groups (1,162 - 1,114 cm^{-1}) [24,25]. Significant spectral changes are observed in the FTIR spectrum of MOSbc-600 (**Figure 4(b)**). The broad absorption band in the 3,600 - 3,200 cm^{-1} region, associated with hydroxyl groups from phenolic and carboxylic functionalities, disappears in MOSbc-600. This change may be attributed to 1 or more of the following processes: (1) Thermal cracking of large tar molecules such as PAHs and phenolics into smaller gaseous compounds including H_2, CH_4, CO, and light hydrocarbons; (2) gas-phase reactions of tar vapors with steam, oxygen, or CO_2, leading to the formation of syngas (H_2 and CO) or complete combustion; and (3) decarboxylation of carboxylic acid groups. The absorption peak around 1,700 cm^{-1}, associated with carboxylic C=O stretching, becomes weaker, suggesting the oxidative decomposition of carboxylic groups with the release of CO and CO_2, as described in Eqs. (15) - (16). This interpretation is further supported by the appearance of a new peak at 2,350 cm^{-1}, corresponding to the asymmetric stretching vibration of O=C=O,

indicative of CO_2 evolution [24]. The rate of CO_2 release increases with higher hemicellulose content and elevated pyrolysis temperatures. Carboxylic acid groups (-COOH) in biomass require a specific activation energy to decompose and release CO_2. As the pyrolysis temperature increases, a larger proportion of molecules acquire sufficient thermal energy to overcome this barrier, thereby accelerating the decarboxylation process. Lignin, which is more thermally stable than hemicellulose, contributes to CO_2 evolution at higher temperatures (400 - 600 °C) through the decomposition of its aromatic carboxyl and methoxyl groups. In contrast, cellulose, which decomposes predominantly between 300 and 400 °C, contributes relatively less to CO_2 evolution.

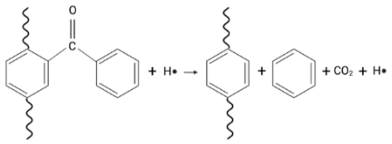

(15)

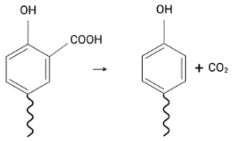

(16)

Following KOH activation, the FTIR spectra exhibit increased absorption intensities at wavenumbers around 3,300 cm^{-1}, corresponding to -OH stretching vibrations, and near 1,700 cm^{-1}, associated with C=O stretching vibrations of carboxyl groups. Additionally, an increase in absorption is observed in the 1,300 - 900 cm^{-1} region, indicative of C-O functional groups. These spectral enhancements are more pronounced in MOSac-600 than in MOSac-500. During KOH activation, residual -OK groups are converted to -OH groups upon washing with water via ion exchange reactions, thereby increasing the hydrophilicity of the activated carbon surface [26]. In this context, higher porosity facilitates more efficient ion exchange, leading to a greater amount of -OH groups and a corresponding reduction in residual potassium (K) content. The presence of oxygen (O) and potassium (K) is further corroborated by EDX analysis (**Figure 3**), which shows a higher oxygen content in MOSac-600 (**Figure 4(e)**) compared to MOSac-500 (**Figure 4(d)**), while the potassium content is lower in MOSac-600. These results align with previous finding by Huang, who reported that KOH-activated wood-based fibers exhibit a high abundance of C-O functional groups.

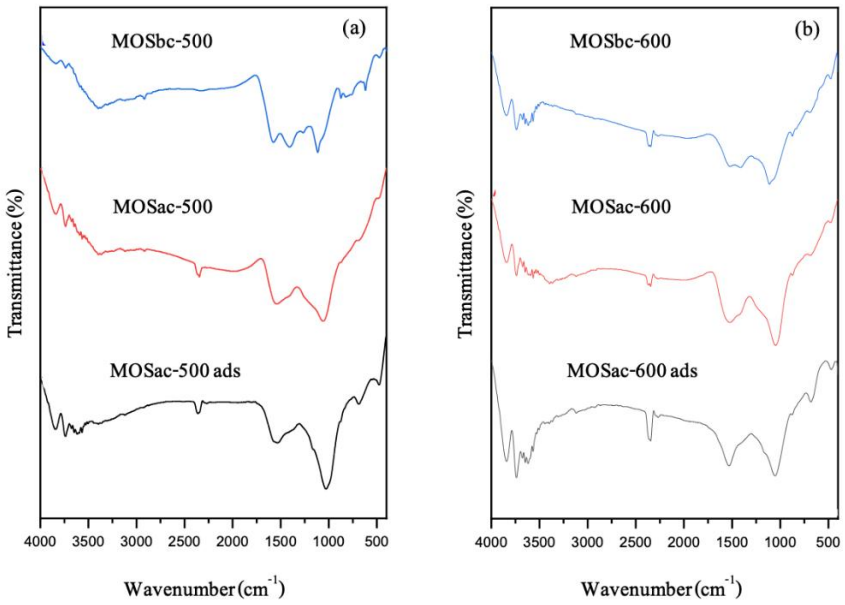

Figure 4 FTIR spectra of MOS biochar (MOSbc), MOS activated carbon (MOSac), and MOS activated carbon after adsorption (MOSac ads) at pyrolysis temperatures of (a) 500 and (b) 600 °C.

Adsorption experiments

The effect of pyrolysis temperature on MV adsorption is illustrated in **Figure 5**. The adsorption capacity of both biochar and AC increased as the pyrolysis temperature was raised from 500 to 600 °C. This enhancement is attributed to the development of additional pores and active sites at higher pyrolysis temperatures, particularly in the AC samples. Adsorption experiments were conducted under various conditions, including different solution pH levels, contact times, and initial dye concentrations. **Figure 5(a)** presents the influence of pH on MV adsorption. Both biochar and AC exhibited an increasing adsorption trend over the pH range of 1 to 11. Notably, MOSac-600 consistently demonstrated higher adsorption capacity than MOSac-500 across all pH values. This is attributed to differences in surface structure and pore characteristics resulting from the different pyrolysis temperatures, as discussed previously. The solution pH plays a critical role in influencing both the surface charge of the adsorbent and the ionization state of the dye molecules. At low pH, the adsorbent surface becomes protonated, as represented by the reaction: -COH + H^+ → -COH_2^+. This protonation leads to the formation of positively charged surface groups, which causes electrostatic repulsion and competitive between H^+ ions and the cationic MV molecules for the available active sites on the AC surface, thereby reducing dye adsorption [19]. As the pH increases, deprotonation occurs according to reaction: -COH → -CO^- + H^+. This results in the formation of negatively charged surface groups, which enhance electrostatic attraction between the adsorbent and the positively charged MV molecules. Consequently, MV adsorption increases with rising pH. The proposed sorption mechanism is illustrated as follows [8]:

MOSbc/MOSac-OH ↔ MOSbc/MOSac -O^- + H^+

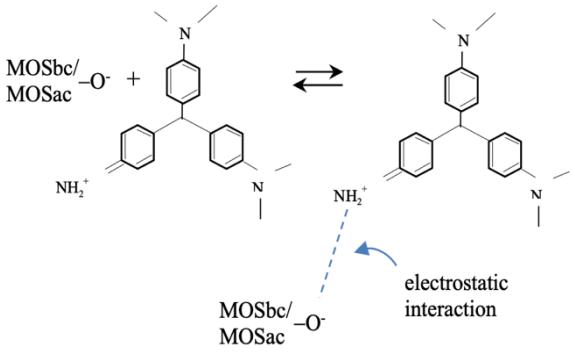

Figure 5(b) illustrates that the adsorption of MV onto both biochar and AC increases rapidly within the first 10 min, followed by a slower rate as equilibrium is approached. This initial rapid uptake is attributed to the abundance of accessible active sites on the adsorbent surfaces at the beginning of the process. As these sites become progressively occupied, the adsorption rate decreases due to repulsive interactions between the already adsorbed dye molecules and those remaining in the solution, which hinders further diffusion. Equilibrium was attained at approximately 120 min for AC and 180 min for biochar. This observation is consistent with findings from previous studies, which suggest that materials with larger surface areas may require longer times to reach equilibrium, as they can accommodate a higher number of dye molecules [8]. The effect of initial dye concentration on MV adsorption is presented in **Figure 5(c)**. The adsorption capacity increases with rising initial MV concentrations but gradually plateaus at higher concentrations. This behavior is attributed to the greater mass transfer driving force at higher initial concentrations, which facilitates the diffusion of dye molecules toward the adsorbent surface and helps overcome mass transfer resistance [19].

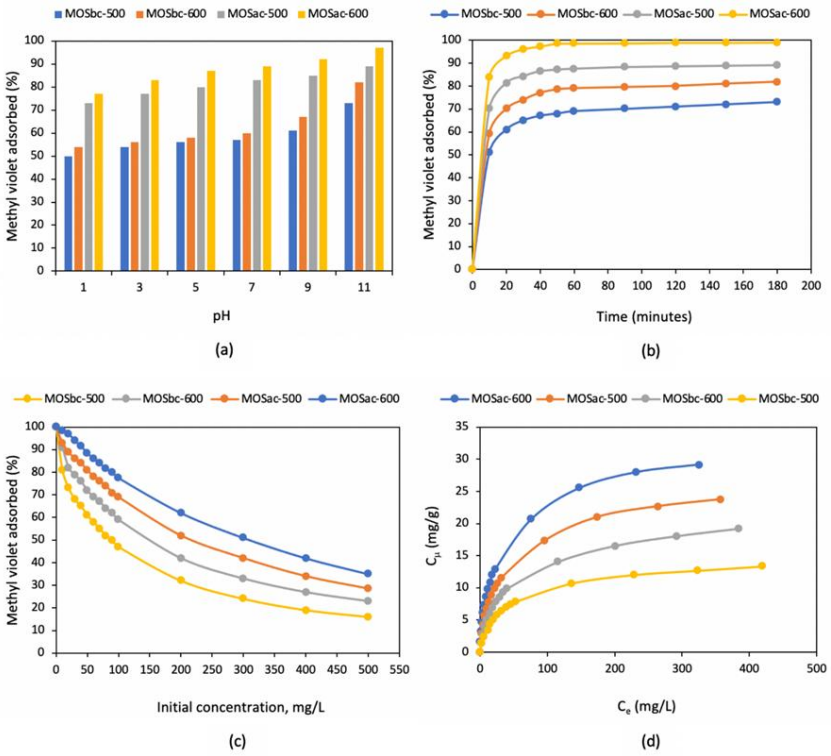

Figure 5 Effect of (a) pH of solution, (b) contact time, (c) initial concentration toward the amount of methyl violet adsorbed, and (d) isotherm adsorption for methyl violet-AC and methyl violet-biochar system.

Adsorption isotherm

An adsorption isotherm characterizes the equilibrium distribution of adsorbate molecules between the liquid and solid phases at a constant temperature. Parameters derived from isotherm models provide critical insights into the adsorption mechanism and are essential for the design and optimization of adsorption processes. The most widely applied models for describing the adsorption of contaminants such as dyes, heavy metals, and organic compounds from aqueous solutions are the Langmuir and Freundlich isotherms. The Langmuir isotherm assumes monolayer adsorption onto a homogeneous surface with energetically identical adsorption sites. According to this model, once a site is occupied by an adsorbate molecule, no further adsorption can occur at that site. Additionally, interactions between adsorbed molecules are considered negligible. The Langmuir isotherm is mathematically expressed as follows [8]:

$$q_e = q_m \frac{K_L C_e}{1 + K_L C_e} \quad (17)$$

where q_m is the maximum adsorption capacity (mg/g), and K_L (L/mg) is the Langmuir constant related to the affinity of the binding sites. Eq. (17) can be linearized as [8]:

$$\frac{C_e}{q_e} = \frac{1}{q_m K_L} + \frac{1}{q_m} C_e \quad (18)$$

A plot of C_e/q_e versus C_e yields a straight line, where the slope is $1/q_m$ and the intercept is $1/q_m K_L$, enabling the determination of Langmuir parameters. In contrast to the Langmuir isotherm, the Freundlich isotherm is an empirical model that describes adsorption on heterogeneous surfaces. It assumes that the adsorption enthalpy decreases logarithmically with increasing surface coverage, reflecting the non-uniform distribution of adsorption energies on the adsorbent surface. The Freundlich isotherm is commonly expressed as follows [8]:

$$q_e = K_F C_e^{\frac{1}{n}} \quad (19)$$

where K_F ((mmol/g) (mmol/L)$^{-n}$) is the Freundlich constant related to the adsorption capacity, and 1/n is heterogeneity factor, indicating adsorption intensity or surface heterogeneity. Eq. (19) can be linearized as:

$$ln\, q_e = ln\, K_F + \frac{1}{n}\, ln\, C_e \quad (20)$$

A plot of $ln\, q_e$ versus $ln\, C_e$ yields a straight line, where the slope is $1/n$ and the intercept is $ln\, K_F$, allowing for the determination of Freundlich parameters. The data presented in **Figure 6** and **Table 3**, which illustrate the linear fitting of experimental results using both the Langmuir and Freundlich isotherm models, indicate that the Langmuir model provides a better fit for all adsorbents. This conclusion is supported by the higher coefficients of determination (R^2) obtained from the Langmuir model, which are closer to unity compared to those derived from the Freundlich model. These findings suggest that MV adsorption follows ideal monolayer behavior, likely governed by a chemisorption on a homogeneous surface [8,9]. Furthermore, the data in **Figure 6** demonstrate that MOSac-600 exhibits the highest adsorption capacity among all materials tested

Table 3 Isotherm parameter and coefficient of determination of MOS biochar-methyl violet and MOS activated carbon-methyl violet system.

Adsorbent	Langmuir isotherm		Freundlich isotherm	
MOSbc-500	q_m	13.966	*1/n*	0.441
	K_L	0.032	K_F	1.199
	R^2	0.993	R^2	0.961
MOSbc-600	q_m	19.841	*1/n*	0.481
	K_L	0.034	K_F	1.445
	R^2	0.988	R^2	0.949
MOSac-500	q_m	24.691	*1/n*	0.478
	K_L	0.041	K_F	1.939
	R^2	0.991	R^2	0.938
MOSac-500	q_m	29.941	*1/n*	0.422
	K_L	0.058	K_F	3.128
	R^2	0.989	R^2	0.888

A review of the existing literature reveals that a wide range of adsorbents have been explored for dye removal, including cassava peel-derived AC [8], polypyrrole-decorated bentonite magnetic nanocomposites (MBnPPy) [25], date seeds [26], oak wood-derived AC [27], coffee husk AC [28], rice husk AC, and AC derived from mangosteen and pomegranate peels [29], as summarized in **Table 4**. In comparison, the MOSac-600 evaluated in the present study demonstrates adsorption performance that is comparable to, or surpasses, that of the aforementioned materials. These findings suggest that the MOSac-600 is a promising candidate for the efficient removal of dye from aqueous solutions.

Table 4 BET surface area and percentage removal of methyl violet by various materials.

Adsorbents	Activator	BET surface area, m^2/g	% Removal	Reference
Cassava peel AC	KOH	457.76	97.00	[8]
Cassava peel AC	H_3PO_4	360.65	98.00	[8]
MBnPPy*	-	335.88	93.41	[27]
Date seeds	-	1.20	62.35	[28]
Oak wood AC	$ZnCl_2$	29.55	92.76	[29]
Coffee husk AC	$ZnCl_2$	613.00	43.00	[30]

Adsorbents	Activator	BET surface area, m^2/g	% Removal	Reference
Rice husk AC	$ZnCl_2$	138.00	28.00	[30]
MPPP-AC**	K_2CO_3	155.00	92.80	[31]
MOSbc-500	KOH	11.75	65.12	this work
MOSbc-600	KOH	53.91	70.23	this work
MOSac-500	KOH	800.53	89.15	this work
MOSac-600	KOH	1,221.56	98.71	this work

*MBnPPy: Polypyrrole-decorated bentonite magnetic nanocomposite.

**MPPP-AC: Mangosteen peel and pomegranate peel activated carbon.

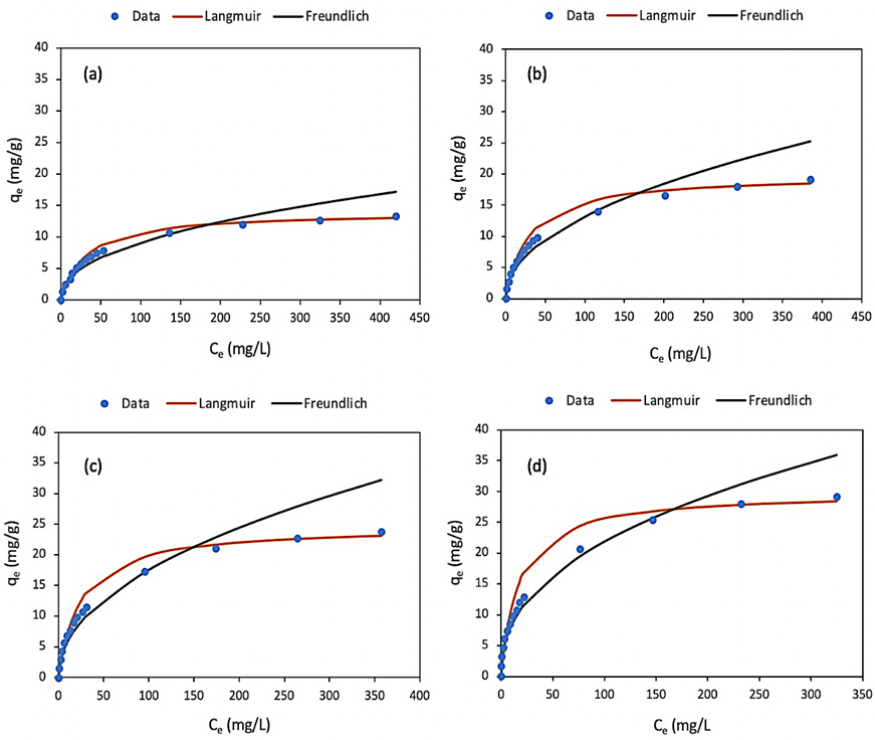

Figure 6 Isotherm adsorption for (a) MOSbc-500 - methyl violet system, (b) MOSbc-600 - methyl violet system, (c) MOSac-500 - methyl violet system, and (d) MOSac-600 - methyl violet system.

Conclusions

This study reports the successful synthesis of activated carbon (AC) from Moringa oleifera stems (MOS) via chemical activation using potassium hydroxide (KOH). The surface morphology of MOSbc-600 (biochar produced at 600 °C) appeared cleaner than that of MOSbc-500 (produced at 500 °C), indicating more effective tar removal at higher pyrolysis temperatures. SEM-EDX and FTIR analysis result revealed higher oxygenated functional groups in MOSac-600 (AC derived from MOSbc-600) compared to MOSac-500 (AC derived from MOSbc-500), contributing to its enhanced adsorption performance. MOSac-600 exhibited a high BET surface area of 1221.56 m^2/g and an average mesopore diameter of 3.42 nm, supporting a methyl violet (MV) adsorption capacity of 29.94 mg/g at pH 11. The equilibrium adsorption data were best described by the Langmuir isotherm model, indicating a homogeneous monolayer adsorption mechanism. Overall, the isotherm modeling and physicochemical characterization confirm that the developed AC is a promising and sustainable adsorbent for the efficient removal of toxic dyes from aqueous environments.

Acknowledgment

The authors are grateful to the Directorate of Research, Technology and Community Service, Ministry of Research, Technology and Higher Education of the Republic of Indonesia for the financial support of this work (Contract number: 117.2.6/UN37/PPK.11/2025).

Declaration of Generative AI in Scientific Writing

No generative artificial intelligence (AI) tools were used in the writing, analysis, or preparation of this manuscript.

CRediT author statement

Widi Astuti: Conceptualization, Methodology, Supervision, Writing - Original draft preparation; **Irene Nindita Pradnya:** Writing - Reviewing and editing; **Triastuti Sulistyaningsih:** Formal analysis, Writing - Reviewing and editing; **Luluk Arvi Cahyaning Suwandi** and **Afifah Sagita Fitria Wati:** Investigation, Writing - Original draft preparation; **Erwan Adi Saputro:** Resources, Writing - Reviewing and editing; **Zulfa Ajrina Fitri:** Visualization, Writing - Reviewing and editing; All authors commented on previous versions of the manuscript, read and approved the final manuscript.

References

[1] R Foroutan, R Mohammadi, A Ahmadi, G Bikhabar, F Babaei and B Ramavandi. Impact of ZnO and Fe_3O_4 magnetic nanoscale on the methyl violet 2B removal efficiency of the activated carbon oak wood. *Chemosphere* 2022; **286**, 131632.

[2] M Ta, Y An, H Yang, C Bai, T Wang, T Zhang, H Cai and H Zheng. Attraction behavior induces the aggregation and precipitation of organic dyes: Improving efficiency through co-treatment strategy. *Journal of Molecular Liquids* 2024; **415**, 126331.

[3] VK Thammannagowda, KGG Shivanna, AK Parameshwarappa, Udayabhanu, P Hanumesh and P Kalappa. Photocatalytic degradation of methylene blue using $CoFe_2O_4/Ag_2WO_4$: Efficiency in degradation of methylene blue dye removal and antimicrobial activity. *Next Materials* 2025; **8**, 100774.

[4] X Yang, C Zhao, Z Zhang, B Zhao, W Wang, X Yang, A Shen and M Ye. Electrochemical degradation of small molecule dyes by TiO_2-decorated polyacrylonitrile nanofiber membranes with superior properties. *Journal of Membrane Science* 2024; **709**, 123132.

[5] T Jamil. Application of ball Clay/MnO_2 based catalytic ozonation process for textile wastewater treatment. *Desalination and Water Treatment* 2024; **318**, 100394.

[6] PR Chowdhury and SK Ray. Synthesis and characterization of polymer-clay nanocomposite membranes for micellar enhanced ultrafiltration of synthetic dyes from water. *Journal of the Taiwan Institute of Chemical Engineers* 2024; **165**, 105768.

[7] V Castro, MLG Fernández, RM Negri, L Lizarraga, A Cánneva, B Aráoz and LMS Medina. Waste based chitosan membranes for dye removal. *International Journal of Biological Macromolecules* 2025; **313**, 143595.

[8] W Astuti, IN Pradnya, R Wulansarie, D Hartanto, T Sulistyaningsih, C Kurniawan, M Hidayah, L Fitriana, MA Mahardhika and EF Irchamsyah. Preparation of magnetic activated carbons from cassava peel using H_3PO_4 and KOH activation by microwave heating for naphthol blue-black adsorption. *Trends in Sciences* 2024; **21(2)**, 7078.

[9] W Astuti, T Sulistyaningsih, D Prastiyanto, Rusiyanto, Lanjar, FI Riayanti, W Astuti, WT Wibowo, AD Handayani and DA Wulandari. Influence of lignocellulosic composition in biomass waste on the microstructure and dye adsorption characteristics of microwave-assisted $ZnCl_2$ activated carbon. *Biomass Conversion and Biorefiney* 2024; **14**, 16681-16697.

[10] M Alrasheedi, TM Alresheedi, AA Algreiby, AS Alnafisah, AS Alresheedi, MAB Aissa, LS Alqarni and A Modwi. Fabrication of green Co_3O_4@g-C_3N_4 nanocomposite for MG dye adsorption. *Diamond and Related Materials* 2025; **157**, 112532.

[11] YAB Neolaka, AA P Riwu, UO Aigbe, KE Ukhurebor, RB Onyancha, H Darmokoesoemo and HS Kusuma. Potential of activated carbon from various sources as a low-cost adsorbent to

remove heavy metals and synthetic dyes. *Results in Chemistry* 2023; **5**, 100711.

[12] D Ionita, M Cristea, SF Cosmulescu, G Predeanu, V Harabagiu and P Samoila. Thermal and viscoelastic responses of selected lignocellulosic wastes: Similarities and differences. *Polymers* 2023; **15(9)**, 2100.

[13] S El Abbadi, H El Moustansiri, M Douma, A Bouazizi, M Baidou, A Elgamouz and N Tijani. Effective elimination of Congo red dye from tannery wastewater using Fe-pillared bentonite: Synthesis, adsorption isotherm, kinetics, and optimization via Box-Behnken design. *Microporous and Mesoporous Materials* 2025; **392**, 113641.

[14] HM Boundzanga, B Cagnon, M Roulet, SD Persis and V Christine. Contributions of hemicellulose, cellulose, and lignin to the mass and the porous characteristics of activated carbons produced from biomass residues by phosphoric acid activation. *Biomass Conversion and Biorefiney* 2022; **12(8)**, 3081-3089.

[15] Y Xu, Y Liu, W Zhan, D Zhang, Y Liu, Y Xu and Z Wu. Enhancing CO_2 capture with K_2CO_3-activated carbon derived from peanut shell. *Biomass and Bioenergy* 2024; **183**, 107148.

[16] T Alfatah, E M Mistar, M Jaber and I Surya. High surface area activated carbon derived from sustainable Kappaphycus alvarezii via 1-step NaOH activation for efficient methylene blue adsorption. *Algal Research* 2025; **90**, 104200.

[17] LEC Chatepa, B Mwamatope, I Chikowe, M Ntholo and KG Masamba. Extraction of phytoconstituents and antioxidant properties from Moringa oleifera L. leaves and seeds from Malawi: A comparative study using deep eutectic and conventional solvents. *Food and Humanity* 2025; **4**, 100635.

[18] ZA Fitri, F Ahmadi, MA Islam, EN Ponnampalam, FR Dunshea and HAR Suleria. A systematic review of extraction methods, phytochemicals, and food application of moringa oleifera leaves using PRISMA methodology. *Food Science and Nutrition* 2025; **13**, e70138.

[19] J Li, D Yang, X Yao, H Zhou, K Xu and L Geng. Slow pyrolysis experimental investigation of biomass tar formation and hydrogen production by tar reforming. *International Journal of Hydrogen Energy* 2024; **52**, 74-78.

[20] Y Zheng, F Fu, Q Liu, H Li, X Zu, X Qiu and W Zhang. Coupling chemical activation and pre-carbonization to produce lignin-derived hierarchical porous carbons with high yields for high-performance hybrid zinc-ion supercapacitors. *Chemical Engineering Science* 2025; **314**, 121830.

[21] D Ionita, M Cristea, SF Cosmulescu, G Predeanu, V Harabagiu and P Samoila. Thermal and viscoelastic responses of selected lignocellulosic wastes: Similarities and differences. *Polymers* 2023; **15(9)**, 2100.

[22] Y Xu, J Wang, G Zhang, X Zhang and Y Zhang. The characteristics and mechanism for the formation of tars from low temperature pyrolysis of lignite. *Journal of the Energy Institute* 2021; **99**, 248-255.

[23] R Janu, V Mrlik, D Ribitsch, J Hofman, P Sedlacek, L Bielska and G Soja. Biochar surface functional groups as affected by biomass feedstock, biochar composition and pyrolysis temperature. *Carbon Resource Conversion* 2021; **4**, 36-46.

[24] Y Huang, E Ma and G Zhao. Thermal and structure analysis on reaction mechanisms during the preparation of activated carbon fibers by KOH activation from liquefied wood-based fibers. *Industrial Crops and Products* 2015; **69**, 447-455.

[25] S Acevedo, L Giraldo and JC Moreno-Pirajan. Kinetic study of CO_2 adsorption of granular type activated carbons prepared from palm shells. *Environmental Science and Pollution Research* 2024; **31**, 39839-39848.

[26] O Oginni, K singh, G Oporto, B Dawson-Andoh, L McDonald and E Sabolsky. Influence of 1-step and 2-step KOH activation on activated carbon characteristics. *Bioresource Technology Reports* 2019; **7**, 100266.

[27] Z Ahamad and A Nasar. Polypyrrole-decorated bentonite magnetic nanocomposite: A green approach for adsorption of anionic methyl orange and cationic crystal violet dyes from contaminated water. *Environmental Research* 2024; **247**, 118193.

[28] NS Ali, NM Jabbar, SM Alardhi, HS Majdi and TM Albayati. Adsorption of methyl violet dye onto a prepared bio-adsorbent from date seeds: Isotherm, kinetics, and thermodynamic studies. *Heliyon* 2022; **8(8)**, e10276.

[29] R Foroutan, R Mohammadi, A Ahmadi, G Bikhabar, F Babaei and B Ramavandi. Impact of ZnO and Fe_3O_4 magnetic nanoscale on the methyl violet 2B removal efficiency of the activated carbon oak wood. *Chemosphere* 2022; **286(1)**, 131632.

[30] M Paredes-Laverde, M Salamanca, JD Diaz-Corrales, E Florez, J Silva-Agredo and RA Torres-Palma. Understanding the removal of an anionic dye in textile wastewaters by adsorption on $ZnCl_2$ activated carbons from rice and coffee husk wastes: A combined experimental and theoretical study. *Journal of Environmental Chemical Engineering* 2021; **9(4)**, 105685.

[31] SA Irwan, AH Jawad, RRR Deris, SA Musa, R Wu and ZA AlOthman. Blended mangosteen/pomegranate peels as a precursor for porous carbon material via microwave assisted-potassium carbonate activation: Box-Benken design optimization for fuchsin basic and methylene violet dyes removal. *Diamond and Related Materials* 2025; **151**, 111846.